Structured empirical waveform contamination in moment tensor inversion of shallow mining seismicity: A synthetic diagnostic framework

S. G. Gomes[1*], A. F. do Nascimento[1], G. S. Leite Neto[2], J. A. S. Fonsêca[3], E. A. S. Menezes[1], and R. A. Fuck[4]

[1] Federal University of Rio Grande do Norte, Department of Geophysics, Natal, Brazil
[2] National Observatory, Rio de Janeiro, Brazil
[3] Polish Academy of Sciences, Institute of Geophysics, Warsaw, Poland
[4] University of Brasília, Geoscience Institute, Brasília, Brazil

Corresponding author and submission contact

S. G. Gomes | sandro_fis@yahoo.com.br

ORCID: https://orcid.org/0009-0009-5218-858X

Preprint status

This manuscript is a non-peer-reviewed preprint submitted to EarthArXiv. This revised version (Version 2) has been prepared for submission to *Geophysical Journal International*.

EarthArXiv DOI: https://doi.org/10.31223/X5QZ2B

Associated research materials

The Online Supplementary Material, numerical results, machine-readable parameter tables, synthetic-test configurations, processing scripts, and reproducibility materials are available through Zenodo:

https://doi.org/10.5281/zenodo.22239316

Structured empirical waveform contamination in moment tensor inversion of shallow mining seismicity: A synthetic diagnostic framework

S. G. Gomes[1], A. F. do Nascimento[1], G. S. Leite Neto[2], J. A. S. Fonsêca[3], E. A. S. Menezes[1] and R. A. Fuck[4]

[1]*Federal University of Rio Grande do Norte, Department of Geophysics, Natal, Brazil*
[2]*National Observatory, Rio de Janeiro, Brazil*
[3]*Polish Academy of Sciences, Institute of Geophysics, Warsaw, Poland*
[4]*University of Brasilia, Geoscience Institute, Brasília, Brazil*
Corresponding author: `sandro_fis@yahoo.com.br`

SUMMARY
Moment tensor inversion of shallow seismicity can be strongly affected by sparse station coverage, uncertain source depth, and waveform mismatch caused by near-surface structural complexity. Conventional synthetic tests usually represent these uncertainties using random noise, but such tests may not reproduce the temporally organised waveform distortions present in local-network data. We develop a diagnostic framework to evaluate this problem using the Jacobina mining district, Brazil, as a realistic test case for shallow mining-induced seismicity.
Synthetic waveforms were contaminated using three complementary strategies: band-limited Gaussian noise as a stochastic reference; recorded local-event waveforms as structured source–path–site contamination; and phase-randomised versions of the same empirical waveforms, preserving their Fourier amplitude spectra while destroying the original temporal phase organisation. We tested two observed six-station configurations and a 12-station combined configuration over source depths of 0.1–5 km. Conventional full-waveform inversion (FW-I) was compared with a P–S segmented inversion (PS-I), in which P- and S-wave windows are treated separately.
Gaussian and phase-randomised contamination produce similar ensemble-level behaviour, with generally smooth increases in moment-tensor rotation as contamination increases. Structured empirical contamination produces a more heterogeneous response: many source–depth–orientation configurations remain weakly affected, whereas a smaller subset develops much larger errors. This behaviour is clearest under FW-I. For the compact six-station network at the highest contamination level, structured contamination produces rotation errors more than 5° larger than the phase-randomised case in 32.1 per cent of realisation-level comparisons, whereas differences below -5° occur in only 7.3 per cent. Differences exceeding $+10^\circ$ occur in 16.4 per cent of comparisons, compared with 2.6 per cent below -10°. Structured temporal organisation therefore preferentially increases the likelihood of large inversion errors rather than uniformly degrading all configurations.
Tests with two additional empirical contaminants reproduce the tendency for larger FW-I errors under structured than phase-randomised contamination, but the depth of maximum susceptibility changes among waveforms. The detailed depth response therefore reflects interactions among source configuration, contaminating waveform, and station geometry. PS-I substantially reduces both the magnitude and frequency of large structured-contamination errors, while the 12-station configuration further suppresses their expression through increased observational redundancy. Source-type discrepancies based on moment-tensor eigenvalues show a weaker and more selective response, indicating that a substantial part of the full-tensor error is associated with changes in recovered orientation. Constraint tests additionally show that solutions can appear stable while remaining systematically biased when an inappropriate source constraint is imposed.
These experiments define a transferable stress-testing framework for shallow moment tensor inversion: establish a stochastic reference, introduce representative structured waveform mismatch, remove its original phase organisation while retaining spectral amplitude, evaluate both typical and large-error behaviour, and test whether acquisition or inversion modifications improve robustness. The numerical thresholds are site-specific, but the diagnostic workflow can be adapted to other shallow and structurally complex seismic environments.

Key words: Inverse theory – Numerical modelling – Earthquake source observations – Induced seismicity – Waveform inversion – Wave propagation

1 INTRODUCTION

Seismicity associated with underground mining provides a natural laboratory for studying source processes under strong anthropogenic perturbations. Excavation-driven stress redistribution, combined with pre-existing geological heterogeneity, can produce seismic responses that differ from those of typical tectonic earthquakes, including swarm-like activity, very shallow source depths, and complex rupture behaviour (Gibowicz & Kijko, 1994). In such environments, reliable characterisation of source mechanisms is important both for understanding the processes governing mining-induced seismicity and for informing hazard mitigation and operational decision-making (Gibowicz & Lasocki, 2001; Barthwal & van der Baan, 2020).

Full moment tensor inversion is widely used in mining settings to distinguish shear slip from tensile opening or collapse-related processes, which may produce considerable non-double-couple components (Lizurek, 2017; Ma et al., 2019). However, source characterisation through moment tensor inversion in shallow mining environments is often challenged by sparse station coverage and waveform distortions associated with near-surface complexity, geological heterogeneity, and path effects that are not adequately represented by simple velocity models or Gaussian-noise assumptions (Duputel et al., 2012; Birnie et al., 2020; Phạm et al., 2024). Understanding and quantifying how these factors affect inversion stability is fundamental for obtaining robust focal solutions and for reliably interpreting and monitoring seismicity in mining districts.

Waveform-based approaches, such as the two-step time-frequency inversion method (Vavryčuk & Kühn, 2012) and the Cut-and-Paste (CAP) technique (Zhao & Helmberger, 1994; Zhu & Helmberger, 1996), improve tolerance to timing mismatches associated with imperfect velocity models. At the same time, it has become increasingly clear that inversion uncertainty reflects not only observational noise but also modelling deficiencies and incomplete physical representations of wave propagation (Duputel et al., 2012).

These concerns have motivated more realistic synthetic assessments. Birnie et al. (2020) showed that benchmarking microseismic imaging and moment tensor inversion methods with white Gaussian noise can yield misleading performance estimates, while more realistic contamination conditions expose instabilities not evident in Gaussian noise tests. Phạm et al. (2024) further demonstrated that full-waveform moment tensor inversion is strongly affected by theory error associated with imperfect three-dimensional Earth structure, especially when structural uncertainties are spatially correlated. In mining settings, Caputa et al. (2021) also showed, through synthetic tests based on the Rudna mine, that realistic station geometry and measured contamination conditions can significantly affect the relative performance of first-motion and waveform-based inversions.

Despite these methodological advances and the growing recognition that realistic noise and forward-model uncertainty can strongly affect moment tensor solutions, an important question remains unresolved: how do systematic waveform distortions that preserve temporal phase structure affect moment tensor stability? Standard synthetic validation commonly relies on random Gaussian noise or incoherent background-noise measures, neither of which presents a structured temporal phase relationship. Although previous studies have shown that realistic noise and correlated theory error can degrade moment tensor inversion more strongly than idealised Gaussian perturbations (Birnie et al., 2020; Phạm et al., 2024), they did not isolate the contribution of temporal phase structure. To our knowledge, no systematic framework has yet explicitly isolated and quantified this contribution under local empirical contamination. This gap is particularly relevant for shallow mining seismicity and for analogous settings such as volcanic and geothermal environments, where coherent scattering, site amplification, near-surface complexity, and structural heterogeneity can introduce systematic waveform distortions across a network.

This study addresses four related questions: (1) Does structured empirical contamination produce degradation beyond that predicted by Gaussian contamination? (2) Does phase randomisation isolate the contribution of preserved temporal phase organisation? (3) Is the additional error expressed only through changes in typical performance, or does structured contamination preferentially increase the occurrence of large-error configurations? (4) How do station coverage and inversion strategy modify these effects?

The Jacobina gold mining district, north-eastern Brazil, is used as a realistic reference case for the station configurations, shallow source-depth range, and empirical waveform contamination examined in the tests. We evaluate band-limited Gaussian contamination, structured empirical contamination constructed from small recorded events, and phase-randomised versions of those empirical waveforms. Conventional full-waveform inversion is compared with a P–S segmented formulation adapted from the CAP concept, and a statistical analysis quantifies the behaviour of moment-tensor error distribution.

Beyond the Jacobina case, the experiments are designed as a transferable stress-testing workflow: site-specific geometry, source-depth range, frequency band, and empirical waveforms can be replaced while retaining the same sequence of stochastic reference, structured empirical perturbation, phase-randomised control, paired comparison, high-error analysis, and mitigation testing.

2 METHODS

2.1 Study Area and Temporary Seismic Network

The Jacobina gold mining district is located in the north-eastern São Francisco Craton, Brazil, and comprises underground mines distributed along the Jacobina Ridge (Fig. 1). The district is characterised by shallow mining-induced seismicity and a structurally heterogeneous geological setting that includes metasedimentary rocks of the Jacobina Group, mapped faults, and mafic dyke systems with dominant north–south and secondary east–west trends (Barbosa & Sabaté, 2004; Santos et al., 2019). The geological description is intentionally limited to the information required to define the synthetic diagnostic framework.

The temporary local network consisted of six three-component short-period stations, including GEObit GEOtiny and Raspberry Shake 3-D instruments, sampling at 100 Hz. Two temporary network geometries were deployed: an initial broad configuration operating from February to April 2022 (Network 1), followed by a more compact configuration operating until August 2023 (Network 2; Fig. 1b). These two geometries, together with an idealised 12-station configuration formed by the union of both layouts, are reproduced in the synthetic tests. The network description is retained only to define the station configurations used in the diagnostic experiments.

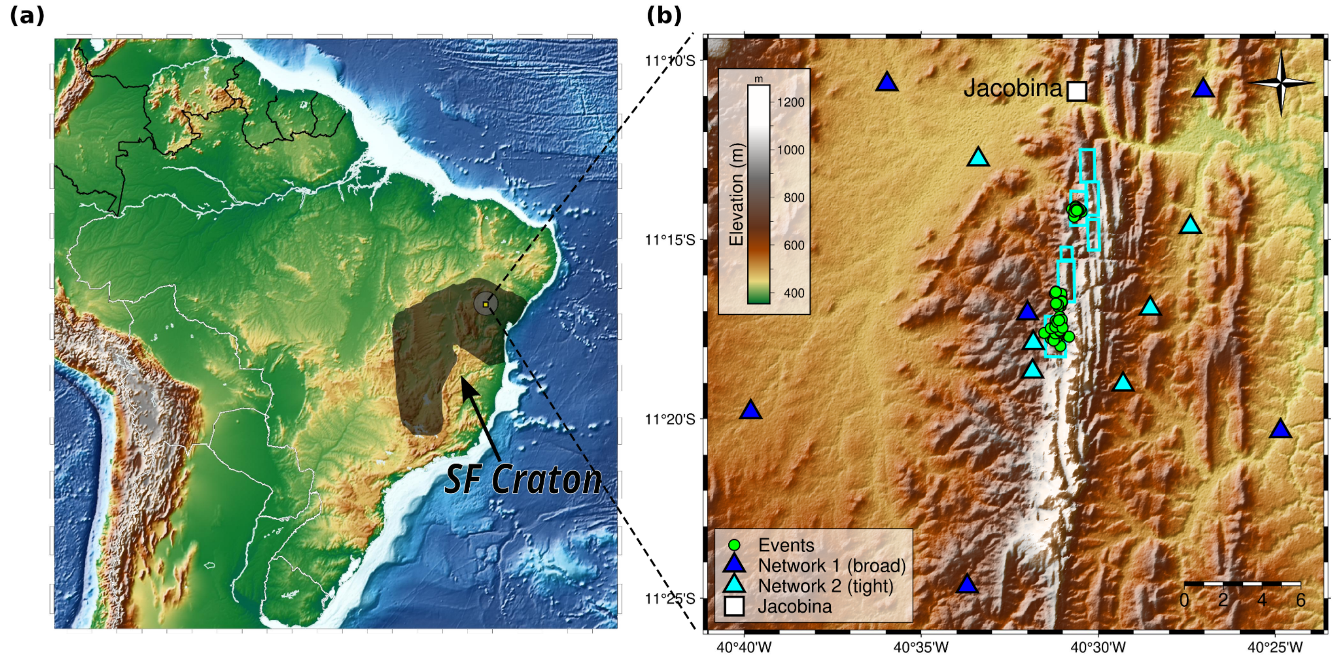

Figure 1. Study area and seismic-network geometry. (a) Regional context of the Jacobina mining district in the São Francisco Craton, north-eastern Brazil. (b) Local topography and seismicity showing the two six-station temporary deployments, relocated events, and mining areas. The idealised 12-station configuration used in the synthetic experiments corresponds to the union of Networks 1 and 2.

Alt text: Two maps locate the Jacobina mining district. The regional map shows Jacobina within the São Francisco Craton in eastern Brazil. The local topographic map shows relocated seismic events concentrated along the central mining corridor, the broad and compact six-station network geometries, and the outlines of the principal mining areas.

2.2 Event Detection, Location and Catalogue Use

We constructed a local event catalogue to provide realistic source-depth constraints, representative waveform examples, and empirical contamination waveforms for the synthetic diagnostic tests. Events were detected using the Python Matching Phase Algorithm (PyMPA) of Vuan et al. (2018), a matched-filter method applied to continuous multi-station waveform data. High-quality templates were windowed around P-wave arrivals and filtered between 2 and 20 Hz. The matched-filter search yielded 373 detections, of which 320 events were retained after visual validation, phase picking, and location-quality screening.

Hypocentral locations were obtained with Hypocenter (Lienert & Havskov, 1995), as implemented in SEISAN (Havskov & Ottemöller, 1999), using a homogeneous velocity model with V_P = 5.9 km s^{-1} and V_P/V_S = 1.69. These values were derived from Wadati analysis and iterative reduction of RMS residuals and location errors. The catalogue spans local magnitudes from approximately M_L = -0.5 to 2.6. Estimated absolute uncertainties are approximately 0.4 km horizontally and 1.3 km vertically; these uncertainties motivated the explicit treatment of source depth as a sensitivity parameter in the synthetic tests.

Relative relocations were performed with HypoDD (Waldhauser & Ellsworth, 2000) using catalogue and cross-correlation differential times. A total of 191 events were relocated in three major mining-sector clusters. These relocations are not interpreted here as a primary seismological result; instead, they define a realistic shallow-source context for the diagnostic experiments and guide the selection of representative recorded events used as empirical waveform contamination.

2.3 Moment Tensor Inversion Framework

Moment tensor inversion was performed using MTUQ, an open-source Python framework for focal mechanism estimation and uncertainty analysis (Thurin et al., 2025). In MTUQ, the full moment tensor is represented as a symmetric 3×3 matrix and decomposed into isotropic and deviatoric components, allowing discrimination between volumetric and complex shear processes. MTUQ implements waveform-based inversion using cross-correlation misfit measures and supports multiple constraint levels, including full moment tensor (FMT), deviatoric (DVT) and pure double-couple (DC) solutions.

Moment tensor space is parametrised using the lune representation (Tape & Tape, 2019), where isotropic and CLVD components are quantified by the parameters δ and γ, respectively. This formulation facilitates systematic exploration of source-type uncertainty and stability. Given the shallow source depths, sparse station coverage, and velocity-model uncertainty in the Jacobina setting, the focus here is on inversion stability and bias rather than on the interpretation of individual source mechanisms.

2.3.1 *Independent P- and S-Wave Inversion (PS-I)*

To address the challenges of local body-wave inversion in this shallow mining setting, we implemented a P–S segmented inversion strategy adapted from the Cut-and-Paste method (Zhao & Helmberger, 1994; Zhu & Helmberger, 1996). CAP separates waveform groups and allows independent timing adjustments to reduce sensitivity to travel-time mismatches associated with imperfect velocity models and source locations. For example, Chang et al. (2019) applied CAP to small-to-moderate earthquakes by separating P waves on the vertical and radial components from S waves on the vertical, radial and transverse components, with independent time shifts between the P- and S-wave groups. In the local-distance setting considered here, surface-wave contributions are weak and the usable signal is dominated by body waves. We therefore adopt the same general segmentation principle but formulate the inversion in terms of independent P- and S-wave windows for full moment tensor analysis.

P- and S-wave windows were defined separately (see the values in Table 1), and the two waveform groups were allowed independent time shifts to accommodate differential propagation effects. Individual misfits were computed for the P and S windows using waveform cross-correlation, and the final misfit was calculated as an equally weighted combination:

$$\chi_{\mathrm{PS-I}} = \chi_P(\Delta t_P) + \chi_S(\Delta t_S). \tag{1}$$

Here, $\chi_{\mathrm{PS-I}}$ is the final misfit function for the PS-I inversion method; χ_P and χ_S are the misfits referred to individual P- and S-wave inversions, respectively; Δt_P and Δt_S are independently optimised time shifts whose absolute values are limited to 0.05 s. This conservative limit was used throughout the synthetic and real-data inversions to accommodate modest timing errors associated with location and velocity-model uncertainty.

This approach is motivated by three considerations: (1) separating P and S waves balances their relative contributions and prevents S-wave amplitude dominance; (2) independent timing adjustments partially accommodate phase-dependent travel-time mismatch without invoking complex 3-D models, including variations in the V_P/V_S ratio; and (3) segmentation provides separate phase-specific constraints and prevents P- and S-wave contributions from being forced into a single coupled waveform fit. The strategy follows the general CAP principle of fitting P- and S-wave groups with independent timing adjustments (Zhao & Helmberger, 1994; Zhu & Helmberger, 1996; Chang et al., 2019), but is implemented here within a full moment tensor framework tailored to local mining-induced seismicity. We evaluated PS-I through synthetic comparisons with conventional full-waveform inversion (FW-I) under the contamination regimes described below.

2.3.2 *Synthetic Waveform Contamination Strategy*

We implemented a three-stage contamination strategy to distinguish stochastic waveform perturbations from structured waveform interference and to isolate the contribution of preserved temporal phase organisation. The first stage used amplitude-controlled, band-limited Gaussian contamination in the 1–5 Hz inversion band. This case provides an incoherent stochastic reference against which the effects of empirical waveform structure can be evaluated.

The second stage used structured empirical contamination derived from small-magnitude events recorded by the local networks. These records retain source radiation, propagation, scattering, and site contributions present in the observed wavefield and are therefore interpreted here as structured source–path–site waveform perturbations rather than as source-free representations of path effects. One representative contaminant was used in the complete synthetic matrix for each network configuration. Because the same recorded waveform was superimposed on synthetics spanning the prescribed source-depth range, detailed depth-dependent responses are interpreted as interactions between the target configuration and a fixed contaminant waveform, rather than as universal functions of source depth.

The third stage used phase-randomised versions of the empirical waveforms to isolate the contribution of their temporal phase organisation. For each station-component trace and realisation, the empirical waveform was transformed to the frequency domain and its amplitude spectrum was retained while the phases were replaced by independent random values,

$$F_{\mathrm{rand}}(\omega) = |F(\omega)| \exp[i\phi_{\mathrm{rand}}(\omega)]\,, \tag{2}$$

where $|F(\omega)|$ is the Fourier amplitude spectrum of the empirical waveform and $\phi_{\mathrm{rand}}(\omega)$ is drawn from a uniform distribution over $[0, 2\pi]$. Conjugate symmetry was imposed so that inverse transformation yielded a real-valued time series. Thus, the phase-randomised case retains the spectral-amplitude content of the empirical contaminant while destroying its original temporal phase relationships.

Contamination was applied before extraction of the inversion windows. For each station-component, the clean synthetic waveform and contaminant were retained as complete unwindowed traces. For scaling purposes only, copies of the two traces were processed using the target-event full-waveform reference window. For empirical contaminants, the contaminant copy was assigned the target synthetic origin and station metadata before this calculation, ensuring that its RMS amplitude was evaluated over the same target-event time interval as the clean synthetic rather than over a window determined from the contaminant event's own source parameters.

The trace-specific scaling was defined as

$$u_{\mathrm{noisy}}(t) = u_{\mathrm{syn}}(t) + \alpha \frac{\mathrm{RMS}_{\mathrm{syn,FW}}}{\mathrm{RMS}_{\mathrm{cont,FW}}} u_{\mathrm{cont}}(t), \tag{3}$$

where u_{syn} and u_{cont} are the complete clean synthetic and contaminant traces, respectively, and the RMS terms are measured over the same target-event full-waveform reference interval. The resulting coefficient was applied to the complete contaminant trace, which was then added sample-by-sample to the complete synthetic trace. Only after this addition was the contaminated parent trace processed to obtain the FW-I, P-wave, and S-wave inversion windows. Consequently, FW-I and PS-I use different windows extracted from the same contaminated waveform realisation; no separate P- or S-specific contaminant was added.

For $\alpha > 0$, this normalisation prescribes a full-waveform reference signal-to-contamination ratio

$$\mathrm{SNR}_{\mathrm{FW}} = \frac{1}{\alpha}. \tag{4}$$

The tested contamination levels $\alpha = 0.2$–1.0 therefore correspond to nominal full-window SNR values of 5–1. The realised SNR within the subsequently extracted P and S windows is not prescribed and may differ because contamination energy is distributed differently in time. This distinction is particularly relevant when comparing structured and phase-randomised contamination under PS-I. Trace-level quality-control checks were used to verify the expected full-window SNR after scaling.

All inversion windows were extracted using the network-specific durations listed in Table 1: P = 1.5 s, S = 2.0 s and FW = 3.5 s for Network 1 and the 12-station configuration, and P = 1.0 s, S = 1.5 s and FW = 2.5 s for Network 2. A 5 per cent post-cut taper was applied consistently. Empirical and synthetic input traces were also required to have compatible sampling, time reference, physical units, and kinematic quantity before addition.

We selected the 1–5 Hz band as a compromise between maintaining sufficient signal-to-contamination ratio and limiting high-frequency waveform complexity not represented by the 1-

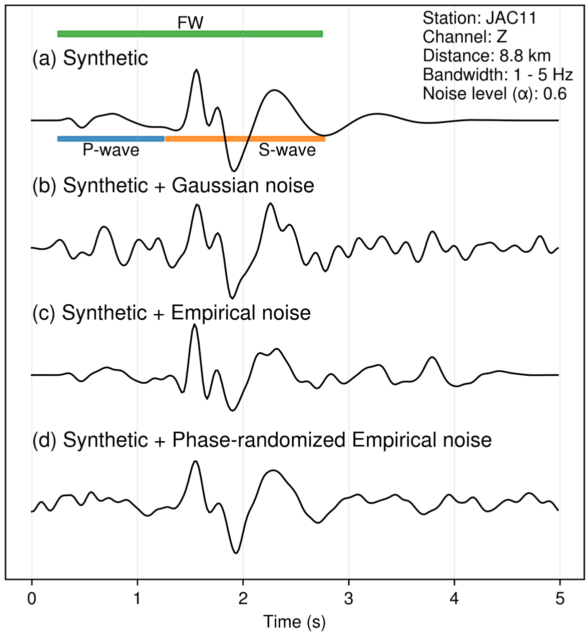

Figure 2. Illustrative waveform effects of the three contamination regimes. (a) Uncontaminated synthetic waveform for a representative source–station pair; coloured bands indicate the P-wave, S-wave, and full-waveform inversion windows. (b)–(d) Gaussian, structured empirical, and phase-randomised empirical contamination, respectively. All examples use $\alpha = 0.6$ and the 1–5 Hz band. Contamination is added to the complete unwindowed synthetic trace before extraction of the FW-I, P-wave, and S-wave windows; consequently, all inversion windows for a given experiment are derived from the same contaminated parent waveform.

Alt text: Four vertically stacked waveform traces compare an uncontaminated synthetic seismogram with Gaussian, structured empirical, and phase-randomised empirical contamination. The same contaminated parent trace is used to extract the inversion windows for each experiment.

D Green's functions. Fig. 2 illustrates the three contamination regimes.

2.3.3 Synthetic Tests and Constraints

Synthetic waveforms were generated by convolving prescribed moment tensors with precomputed Green's functions calculated using Computer Programs in Seismology (Herrmann, 2013). Source depths ranged from 0.1 to 5 km. The horizontal source–receiver geometry for each contamination experiment was anchored to the epicentre of the empirical-contaminant event used in that experiment. For each six-station network, three small recorded events were selected as empirical contaminants. Their epicentres, together with the corresponding station coordinates, defined the epicentral distances and source–station azimuths used to calculate the Green's functions. One event was used in the complete synthetic matrix, whereas the other two were used in the reduced multi-contaminant robustness experiment. Synthetic source depth was varied independently over the prescribed depth grid and was therefore not fixed to the depth estimated for the empirical contaminant.

For the 12-station configuration, two spatially nearby empirical events were selected whose recordings jointly provided coverage of the complete station union. Their waveforms were combined to form a virtual empirical contaminant recorded by all twelve stations, and the resulting horizontal source–receiver geometry was used, together with the independently prescribed synthetic source depths, to calculate the Green's functions for the 12-station experiments. For all configurations, Green's functions and uncontaminated synthetics were generated using the same homogeneous 1-D velocity model adopted for hypocentral location, with $V_P = 5.9$ km s^{-1} and $V_S \simeq 3.49$ km s^{-1}. Synthetic traces were sampled at 0.02 s with 512 samples and used a Dirac delta source-time function. The baseline synthetic experiments therefore contain no intentional forward-model mismatch; structured mismatch enters through the added empirical waveform.

The synthetic test suite considered four prescribed source cases: ISO-dominant (ISO), CLVD-like (CLVD), mixed (MIX), and double-couple (DC), together with normal, reverse, and strike-slip orientations. The ISO and CLVD labels denote prescribed positions on the moment-tensor lune rather than mathematically pure end members; DC is the pure double-couple case. The corresponding lune coordinates are provided in Supplementary Table S1. The final magnitude of the synthetic source was fixed at $M_W = 2$.

Gaussian and phase-randomised contamination were evaluated with 15 independent realisations for each network–source–orientation–depth–α configuration, whereas the structured empirical experiment is deterministic for a given contaminant and configuration. For the principal source- and depth-dependent comparisons, the 15 stochastic realisations were first collapsed using the median for each identical configuration. This gives each prescribed configuration the same weight as the corresponding deterministic structured experiment and provides a robust estimate of its typical stochastic-control response.

Inversion performance was quantified primarily using the moment-tensor rotation angle ω between the prescribed and recovered tensors (Tape & Tape, 2012). Following the spherical eigenvalue-space representation of moment-tensor source type (Tape & Tape, 2012; Tape & Tape, 2019), source-type recovery was quantified here by the angular distance between the normalised ordered eigenvalue triplets of the prescribed and recovered tensors,

$$\theta_\lambda = \cos^{-1}\left(\widehat{\boldsymbol{\lambda}}_{\text{true}} \cdot \widehat{\boldsymbol{\lambda}}_{\text{rec}}\right), \tag{5}$$

where $\widehat{\boldsymbol{\lambda}}$ denotes the ordered eigenvalue triplet normalised to unit Euclidean length. Because source type is represented by the normalised eigenvalues whereas tensor orientation is carried by the eigenvectors, θ_λ provides an orientation-independent measure of source-type discrepancy. Rotation-angle curves and heatmaps are summarised by medians across the relevant configurations. For θ_λ, the figures report the mean and one standard deviation across configurations after the realisation-level median collapse.

Comparisons between contamination regimes were performed on matched configurations. Thus,

$$\Delta\omega_{E-G} = \omega_{\text{structured}} - \omega_{\text{Gaussian}} \tag{6}$$

and

$$\Delta\omega_{E-RD} = \omega_{\text{structured}} - \omega_{\text{randomised}} \tag{7}$$

were calculated configuration by configuration before aggregation. Analogous paired differences were calculated for θ_λ.

Because a configuration-wise median can conceal a smaller population of large errors, we also performed a complementary distributional analysis at $\alpha = 1$. For each source–depth–orientation configuration, the single deterministic structured result was paired separately with each of the 15 Gaussian or phase-randomised realisations. This produced 1620 paired differences for each network–method–comparison combination (4 source types $\times$ 3 orientations

$\times$ 9 depths $\times$ 15 stochastic realisations). Positive and negative exceedance probabilities were evaluated at symmetric 5° and 10° thresholds for both ω and θ_λ, together with distribution quantiles. These thresholds are descriptive diagnostics for the present synthetic ensemble rather than universal acceptance criteria. Because the 15 paired differences within one configuration share the same structured solution, they were treated as clustered realisations rather than independent source configurations. We therefore also calculated, for each configuration i, the fraction $p_i(\Delta > 0)$ of stochastic realisations for which the structured result produced the larger error. Complete distributional statistics are provided in Supplementary Tables S2–S3 and Figs S7–S8.

The complete three-contamination matrix was evaluated for Network 1, Network 2, and the 12-station configuration. To test whether the phase-structure response depended critically on the empirical event selected for the main matrix, two additional empirical contaminants and their phase-randomised counterparts were tested for Networks 1 and 2. This limited robustness experiment used the common non-ISO source families (CLVD, MIX, and DC), the three faulting orientations, source depths of 0.5, 2.0, and 4.0 km, and $\alpha = 1$ for the direct structured-versus-randomised comparison. For this robustness comparison, the reported statistic is the mean paired $\Delta\omega_{E-RD}$ with ± 1 standard deviation across the nine matched source–orientation configurations at each depth.

Full moment tensor inversion was used throughout the principal experiments. Deviatoric and double-couple constraints were evaluated only in the dedicated constraint-sensitivity experiment. To distinguish persistent mechanism bias from contamination sensitivity, that analysis compares (i) the mean across contamination levels of the median ω across configurations and (ii) the paired change between $\alpha = 0$ and $\alpha = 1$,

$$\Delta\omega_{0\to1} = \mathrm{median}_i \left[\omega_i(\alpha = 1) - \omega_i(\alpha = 0)\right], \tag{8}$$

where i indexes matched source configurations.

In PS-I, P- and S-window misfits were optimised independently using the timing limits described in Section 2.3.1. Table 1 summarises the principal synthetic-test settings.

2.3.4 *Real-Data Diagnostic Inversion*

A representative M_L 1.2 event recorded by Network 2 (stations JAC7–JAC12) was analysed to determine whether the synthetic diagnostics were consistent with the observed sparse-network data. Waveforms were processed in the same 1–5 Hz band and inverted with the same Green's functions, component weighting, window lengths, and maximum time shifts used in the corresponding Network 2 synthetic tests.

Full moment tensor solutions were searched over source depths from 0.1 to 2.5 km at 0.2 km intervals and moment magnitudes from M_W 1.0 to 1.4 at 0.1-unit intervals. Both FW-I and PS-I were applied. The real-data example is used only to illustrate method- and depth-dependent non-uniqueness and is not interpreted as evidence for a preferred source mechanism.

3 RESULTS

3.1 Synthetic Validation

3.1.1 *Gaussian Noise Baseline*

Gaussian contamination provides the stochastic reference against which the structured experiments are evaluated. For the CLVD-like, mixed, and DC source cases, both FW-I and PS-I show progressive degradation as α increases, whereas the ISO-dominant case remains comparatively stable in full-tensor orientation. In Network 1, median FW-I rotation angles at $\alpha = 1$ are approximately 8.5–9.2° for the non-ISO cases, while the ISO-dominant case remains near 5° (Fig. 3a). Network 2 shows the same overall behaviour but somewhat larger FW-I errors for the most sensitive cases, reaching approximately 9.2–12.2° at $\alpha = 1$ (Fig. 4a). The 12-station configuration reduces the largest Gaussian-contamination rotations, with non-ISO median FW-I values of approximately 6.4–8.2° at $\alpha = 1$ (Supplementary Fig. S1a).

The Gaussian depth response is comparatively smooth. At $\alpha = 1$, Network 1 PS-I median ω varies from approximately 7.6° to 10.7° across the common depth grid, with its largest value at 0.5 km (Fig. 3b). Network 2 is more uniform, with PS-I medians confined to approximately 7.4–9.1° and no persistent depth-localised anomaly (Fig. 4b). Overall, the Gaussian response, for FW-I and PS-I formulations, varies more smoothly with depth than the structured empirical-contamination response.

Source-type discrepancy shows the expected contamination-dependent increase for the non-ISO cases. After the stochastic realisations are collapsed by their configuration-wise median, mean θ_λ for CLVD-like, MIX, and DC cases in Network 1 increases from approximately 1–2.5° at $\alpha = 0.2$ to approximately 4.5–6° at $\alpha = 0.8$, whereas the ISO-dominant case changes little (Fig. 3c). Network 2 shows a similar tendency (Fig. 4c), and the 12-station configuration generally reduces the increase, particularly under PS-I (Fig. S1c).

3.1.2 *Effects of Structured Empirical Contamination*

Compared with the Gaussian reference, structured empirical contamination produces larger and more configuration-dependent moment-tensor rotations, with the clearest separation occurring under FW-I (Figs 5 and 6). In Network 1 at $\alpha = 1$, median FW-I ω under structured contamination is 11.4°, 10.6°, and 11.9° for the CLVD-like, MIX, and DC cases, respectively, compared with 8.5°, 9.0°, and 9.2° under Gaussian contamination. The ISO-dominant case changes only from 4.8° to 5.4°. Network 2 shows a stronger separation for the CLVD-like and MIX cases: their FW-I medians increase from 9.2° and 9.3° under Gaussian contamination to 12.6° and 13.6° under structured contamination. The DC case increases more modestly, from 12.2° to 13.1°, while the ISO-dominant case again changes little.

The paired depth comparison $\Delta\omega_{E-G}$ shows that the additional structured-contamination response is strongly depth-dependent. In Network 1 at $\alpha = 1$, the largest median FW-I differences occur at shallow depths, reaching approximately 3.5° at 0.3 km and 2.3° at 0.5 km, while differences at most other depths are smaller and become slightly negative at 3 km (Fig. 5b). Network 2 exhibits a much stronger shallow response, with median paired differences of approximately 8.3° at 0.3 km and 7.6° at 0.5 km. The excess decreases sharply by 0.8–2 km, becomes slightly negative at 3 km, and increases again more modestly at 4–5 km (Fig. 6b). The main-contaminant response therefore does not define a single persistent depth interval of maximum degradation.

The contrast is considerably weaker under PS-I. In Network 1 at $\alpha = 1$, structured PS-I medians are 5.3°, 8.1°, 10.5°, and 9.2° for the ISO-dominant, CLVD-like, MIX, and DC cases, compared with Gaussian values of 5.3°, 9.2°, 8.9°, and 9.2°. Only the MIX case therefore shows a clear source-aggregated increase (Fig. 5a). Network 2 retains a measurable PS-I excess for MIX and DC but

Table 1. Inversion parameters used in this study. Full source-case, geometry, and distributional-analysis settings are listed in Supplementary Table S1.

Parameter	Setting
Green's functions	CPS wavenumber integration
Velocity model	Homogeneous 1-D model; $V_P = 5.9$ km s^{-1}; $V_S \simeq 3.49$ km s^{-1}
Frequency band	1–5 Hz
Inversion methods	FW-I; PS-I
Constraint levels	FMT (principal tests); DVT and DC (Section 3.1.6 only)
Synthetic depth grid	0.1–5.0 km, with denser sampling at shallow depths
Station configurations	Broad six-station (Network 1); compact six-station (Network 2); 12-station union
Contamination models	Gaussian (15 realisations); structured empirical (deterministic representative contaminant); phase-randomised empirical (15 realisations)
Contamination scaling	$\alpha = 0.0, 0.2, 0.4, 0.6, 0.8, 1.0$; nominal $\mathrm{SNR_{FW}} = 1/\alpha$ for $\alpha > 0$
Time windows (Network 1 and 12-station)	P: 1.5 s; S: 2.0 s; FW: 3.5 s
Time windows (Network 2)	P: 1.0 s; S: 1.5 s; FW: 2.5 s
Post-cut taper	5 per cent
Maximum time shift	0.05 s
Primary mechanism-error metric	Rotation angle ω
Source-type discrepancy	Eigenvalue angle θ_λ
Distributional analysis	$\alpha = 1$; common nine-depth grid; all 15 stochastic realisations retained
Additional-contaminant test	Networks 1–2; CLVD, MIX, DC; 0.5, 2.0, 4.0 km; $\alpha = 1$ comparison

little change for CLVD (Fig. 6b). Across depth, paired PS-I differences are generally much smaller than their FW-I counterparts, although local positive and negative departures remain. P–S segmentation therefore suppresses the strongest structured-contamination response without eliminating configuration dependence.

The source-type metric θ_λ is also more heterogeneous than ω. Under FW-I at $\alpha = 1$, structured contamination increases mean θ_λ from $5.9 \pm 2.3°$ to $8.9 \pm 6.6°$ for the Network 1 CLVD-like case and from $6.6 \pm 3.5°$ to $9.8 \pm 7.9°$ for DC(Fig. 5c). In Network 2, the corresponding CLVD-like increase is from $7.0 \pm 2.5°$ to $11.5 \pm 7.3°$ and the DC increase from $7.9 \pm 3.0°$ to $11.0 \pm 8.5°$ (Fig. 6b). PS-I differences are smaller and not consistently positive. Detailed absolute structured-contamination maps using the complete 13-depth grid are provided in Supplementary Figs S2–S4.

3.1.3 Role of Preserved Temporal Phase Structure

Phase randomisation provides the direct diagnostic for determining whether the additional degradation under empirical contamination depends on preserved temporal waveform organisation. Because the empirical Fourier-amplitude spectrum is retained while the original phase relationships are destroyed, the convergence of the phase-randomised results towards the Gaussian response indicates that spectral amplitude alone is insufficient to reproduce the structured-contamination effect.

For both six-station networks, phase-randomised empirical contamination closely follows the Gaussian response at the ensemble level, whereas structured empirical contamination produces larger FW-I errors for several non-ISO source cases (Figs 7 and 8). At $\alpha = 1$, Network 2 median FW-I ω is $12.6°$ for the CLVD-like case and $13.6°$ for MIX under structured contamination, compared with approximately $9°$ under phase-randomised contamination. Network 1 shows a weaker but comparable separation.

The paired $\Delta\omega_{E-RD}$ depth response follows the same pattern. Network 2 reaches approximately $7.8°$ at 0.3 km and $7.4°$ at 0.5 km under FW-I, whereas Network 1 shows a smaller and more heterogeneous pattern with both positive and negative depth intervals. The sign changes are important: preserved temporal organisation does not increase ω for every configuration. Rather, it changes which configurations become strongly susceptible, a behaviour quantified explicitly by the distributional analysis in Section 3.1.4.

The main phase-structure result is robust to the choice of empirical waveform. Two additional contaminants were tested using the common non-ISO reduced grid (Supplementary Fig. S6). The depth-averaged mean FW-I $\Delta\omega_{E-RD}$ remains positive for all three contaminants in both six-station networks: approximately $2.2°$, $5.2°$, and $1.6°$ for Events 1–3 in Network 1 and $5.4°$, $2.7°$, and $2.7°$ in Network 2. The depth of maximum excess nevertheless migrates among contaminants. Event 2, for example, produces $11.9 \pm 9.6°$ at 0.5 km in Network 1 but its largest Network 2 response at 4 km ($6.6 \pm 4.9°$). Thus, the existence of an ensemble-level coherence-related FW-I excess is reproducible, whereas its magnitude and depth localisation are waveform- and geometry-dependent.

3.1.4 Distributional Response and High-Error Susceptibility

The configuration-wise median comparisons describe the typical response to structured contamination but do not fully characterise the distribution of possible errors. We therefore retained all 15 stochastic realisations and paired the deterministic structured result separately with each Gaussian or phase-randomised realisation for the same source–depth–orientation configuration. Supplementary Figs S7–S8 and Tables S2–S3 show the resulting two-sided exceedance distributions at $\alpha = 1$.

For the full moment-tensor rotation ω, the realisation-level distributions are positively asymmetric under FW-I. In Network 1, 23.4 per cent of structured-minus-randomised differences exceed $+5°$ whereas 7.9 per cent fall below $-5°$; the corresponding proportions beyond $\pm 10°$ are 7.7 and 2.3 per cent. Network 2 shows a stronger asymmetry: 32.1 per cent exceed $+5°$ compared with 7.3 per cent below $-5°$, and 16.4 per cent exceed $+10°$ compared

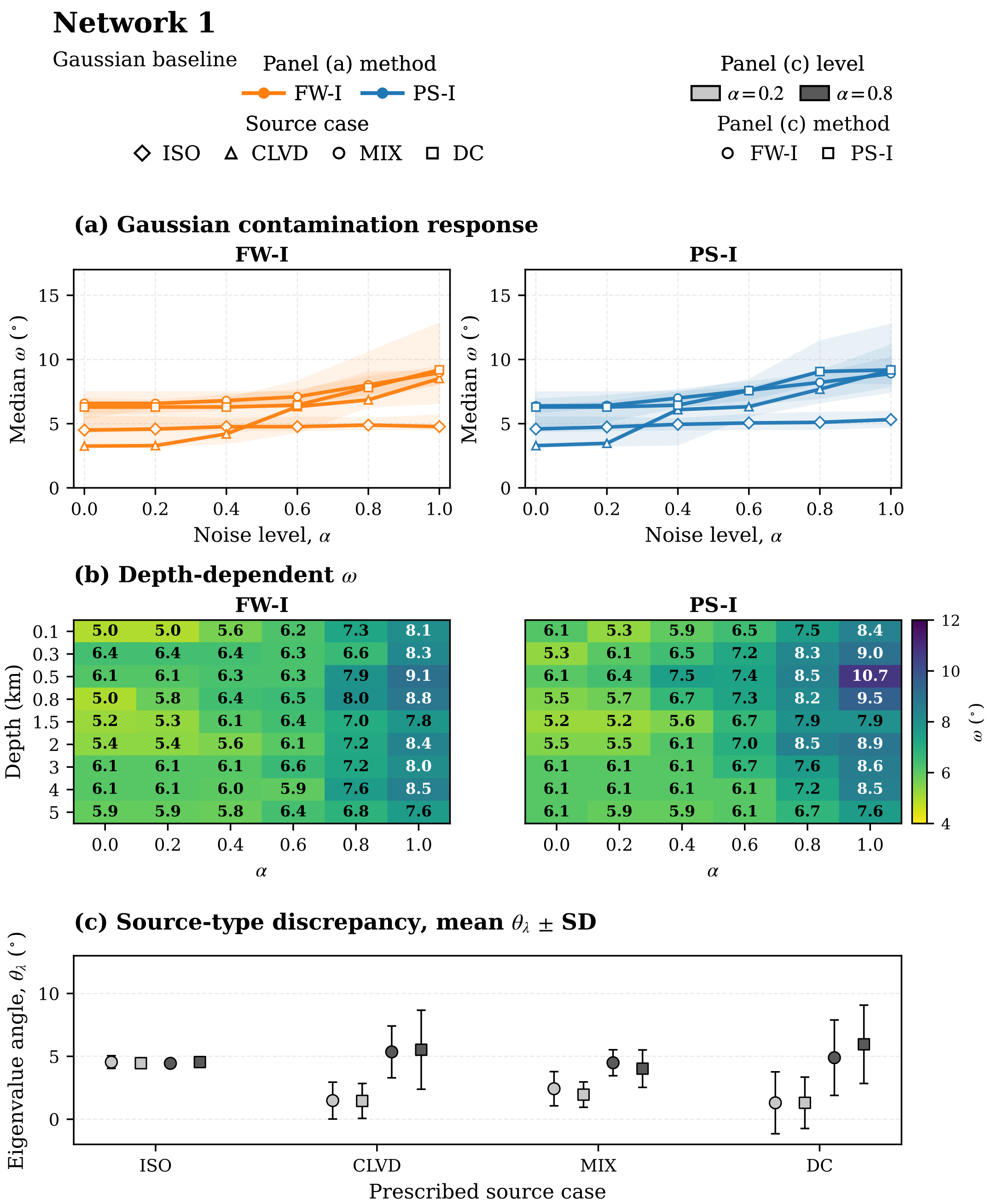

Figure 3. Gaussian-contamination baseline for Network 1. (a) Median moment-tensor rotation angle ω as a function of contamination level α for the ISO-dominant (ISO), CLVD-like (CLVD), mixed (MIX), and double-couple (DC) prescribed source cases under FW-I and PS-I. Independent Gaussian realisations are first collapsed by their configuration-wise median. (b) Median ω as a function of source depth and α for FW-I and PS-I. (c) Source-type discrepancy measured by the eigenvalue angle θ_λ at $\alpha = 0.2$ and 0.8. Points show the mean across source-depth-orientation configurations and error bars denote ± 1 standard deviation.

Alt text: Multi-panel figure showing the response of Network 1 to Gaussian contamination. Rotation-angle curves increase progressively with contamination level for the CLVD-like, mixed, and double-couple source cases, while the ISO-dominant case changes less. Depth-dependent heatmaps show a comparatively smooth response without a persistent narrow depth interval of anomalous degradation. The eigenvalue-angle panel shows increasing source-type discrepancy for the non-ISO source cases as contamination increases, with variability among source configurations.

with 2.6 per cent below -10°. The structured-versus-Gaussian comparison shows the same qualitative imbalance. Thus, modest configuration-level medians coexist with a substantial population of much larger positive differences: structured empirical contamination preferentially increases high-error outcomes rather than simply broadening the paired distribution symmetrically.

The within-configuration analysis confirms that this behaviour is not produced solely by pooling isolated stochastic realisations. For Network 2 FW-I, the median configuration has an exceedance

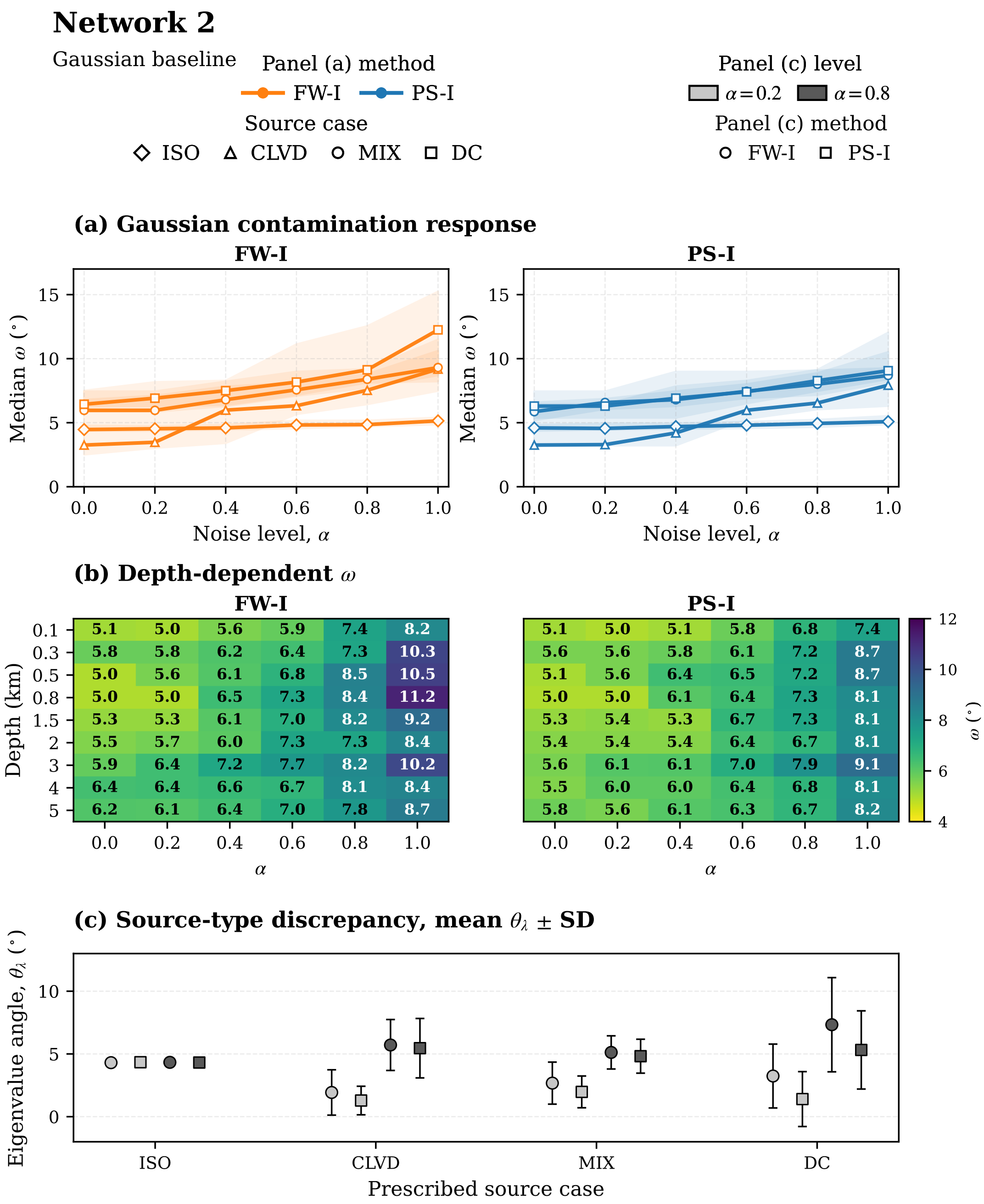

Figure 4. Gaussian-contamination baseline for Network 2. Panel definitions and statistical summaries are the same as in Fig. 3.

Alt text: Multi-panel figure showing the Gaussian-contamination response for Network 2. Full-waveform and P–S segmented inversions generally show increasing moment-tensor rotation with contamination level. The ISO-dominant source remains comparatively stable, whereas the non-ISO sources show larger degradation. Depth variations remain relatively smooth, although Network 2 reaches somewhat larger full-waveform rotation angles than Network 1 for selected source cases. Eigenvalue-angle results show increasing source-type discrepancy for the non-ISO sources.

fraction of $P(\Delta\omega_{E-RD} > 0) = 0.80$, and 51.9 per cent of configurations have $P \geq 0.8$. For the corresponding Network 1, the respective values are 0.60 and 40.7 per cent. P–S segmentation substantially reduces the imbalance. In Network 2, $P(\Delta\omega_{E-RD} > 5^\circ)$ decreases from 32.1 per cent under FW-I to 14.3 per cent under PS-I, and the $\pm 10^\circ$ PS-I tails are approximately balanced. Network 1 shows the same general tendency.

The 12-station network further compresses the full-tensor high-error tail. Under FW-I, $P(\Delta\omega_{E-RD} > 5^\circ)$ decreases to 15.9 per cent and $P(\Delta\omega_{E-RD} > 10^\circ)$ to 4.3 per cent. Under PS-I, only 3.1 per cent of paired differences exceed $+5^\circ$ and none exceeds $+10^\circ$. Increased station coverage therefore reduces not only the median structured-contamination excess but also the occurrence of large-error configurations.

The eigenvalue-angle metric θ_λ shows a related but weaker distributional response. Under FW-I, Network 1 and Network 2 structured-minus-randomised differences exceed $+5^\circ$ in 22.6 and 27.0 per cent of comparisons, respectively, compared with 11.7 and

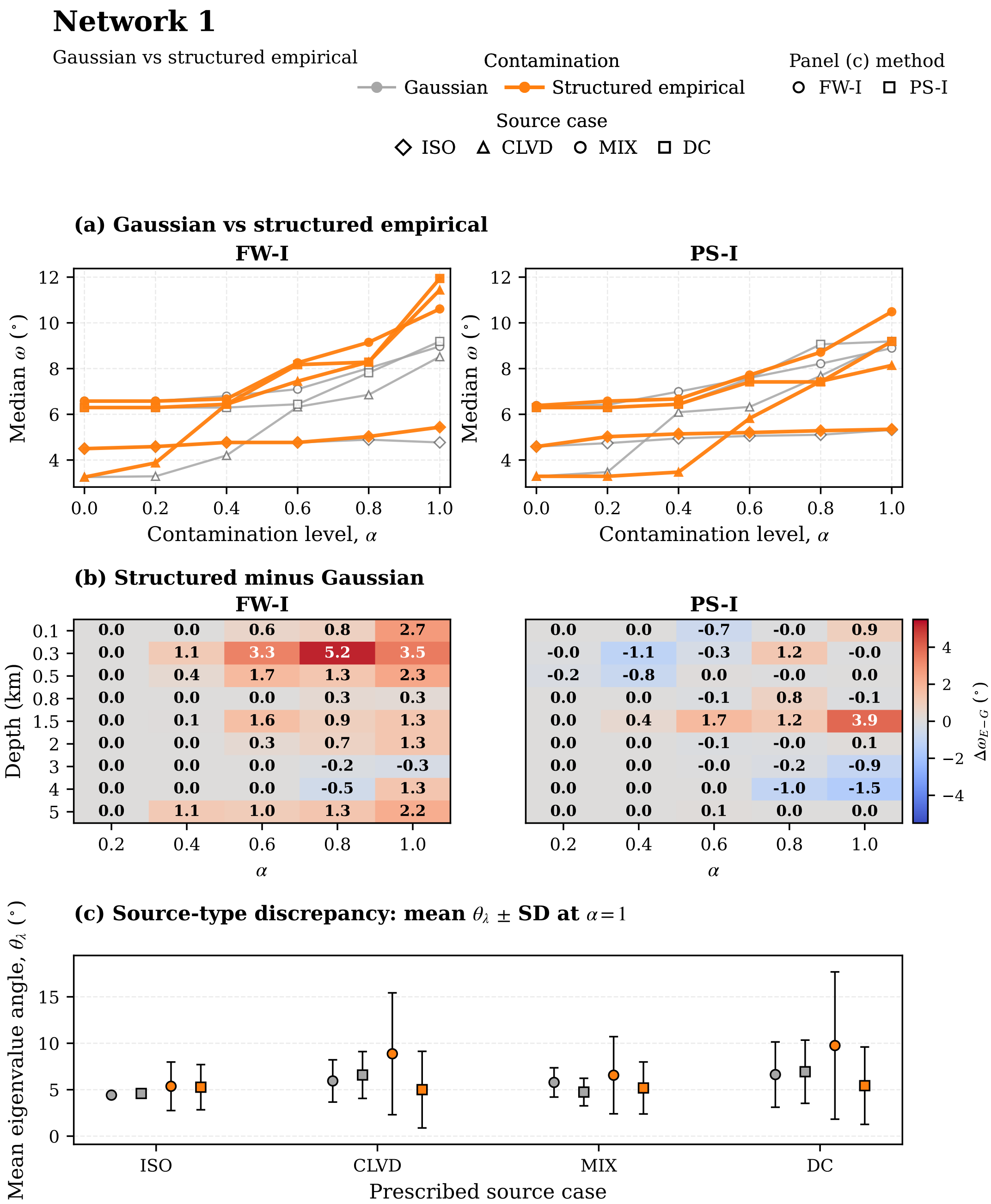

Figure 5. Gaussian versus structured empirical contamination for Network 1. (a) Median rotation angle ω as a function of α for the prescribed source cases under Gaussian and structured empirical contamination, shown separately for FW-I and PS-I. (b) Median paired difference $\Delta\omega_{E-G} = \omega_{\text{structured}} - \omega_{\text{Gaussian}}$ for matched source-depth-orientation configurations. (c) Eigenvalue-angle discrepancy θ_λ at $\alpha = 1$ under Gaussian and structured empirical contamination. Points show configuration means and error bars denote ± 1 standard deviation.

Alt text: Multi-panel comparison of Gaussian and structured empirical contamination for Network 1. Full-waveform rotation angles are generally larger under structured empirical contamination for the more sensitive non-ISO source cases, especially at high contamination levels. Paired depth maps show positive structured-minus-Gaussian rotation differences at several depths, with the strongest response concentrated in selected shallow configurations. P–S segmentation substantially reduces these differences. Eigenvalue-angle results show a more variable and source-dependent structured-contamination effect than the full-tensor rotation.

12.7 per cent below $-5°$. For the 12-station network these proportions decrease to 19.1 and 9.0 per cent. The positive asymmetry largely disappears under PS-I and can reverse in the broader network configurations. This contrast is consistent with the different information carried by the two metrics: ω compares the complete tensors and is sensitive to changes in both orientation and eigenvalue structure, whereas θ_λ isolates source-type eigenvalue discrepancy. The stronger ω response therefore indicates that a substantial component of the structured-contamination error is associated with changes in recovered tensor orientation, while large source-type changes occur in a more restricted subset of configurations.

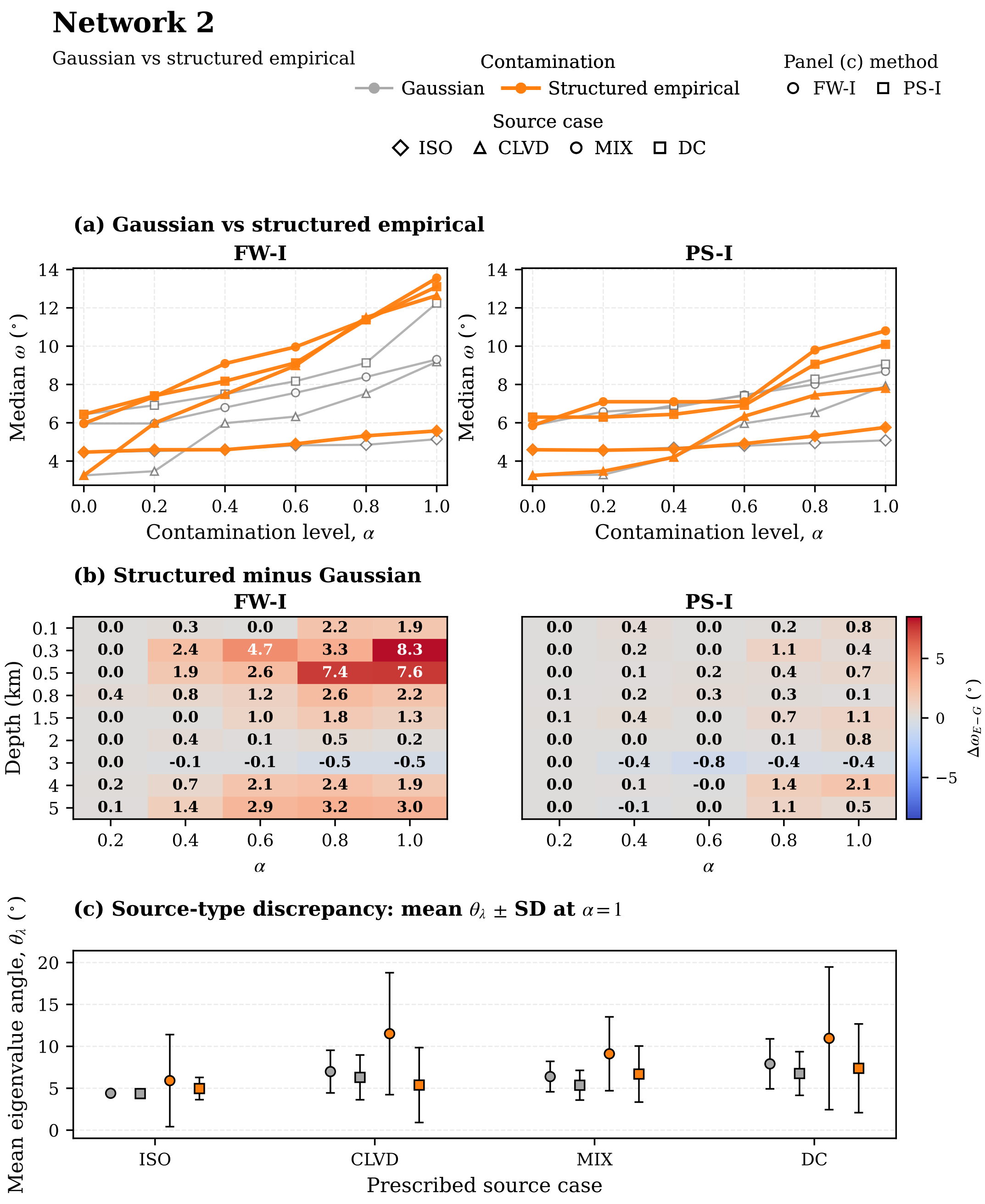

Figure 6. Gaussian versus structured empirical contamination for Network 2. Panel definitions and statistical summaries are the same as in Fig. 5.

Alt text: Multi-panel comparison of Gaussian and structured empirical contamination for Network 2. Structured contamination produces substantially larger full-waveform rotation errors than Gaussian contamination for several non-ISO source cases. The paired depth comparison shows a pronounced positive structured-minus-Gaussian excess at shallow depths, with smaller residual differences at intermediate and greater depths. P–S segmentation strongly suppresses the shallow full-waveform excess. Source-type eigenvalue-angle changes are present but are less systematic than the full-tensor rotation response.

3.1.5 Role of Network Geometry

The network comparison shows that station geometry controls the expression of structured waveform contamination rather than defining a single characteristic depth of failure. Under Gaussian contamination, differences among the station configurations are comparatively modest and the 12-station network mainly reduces the absolute error and configuration-to-configuration spread. Under structured empirical contamination, geometry exerts a stronger control on the depth-dependent response.

For the main empirical contaminant, both six-station networks exhibit substantial shallow FW-I sensitivity, although the amplitude differs between them. The additional-contaminant tests demonstrate that these depth patterns are not fixed network properties: the location of maximum coherent-minus-randomised excess migrates among 0.5, 2, and 4 km as the contaminating waveform

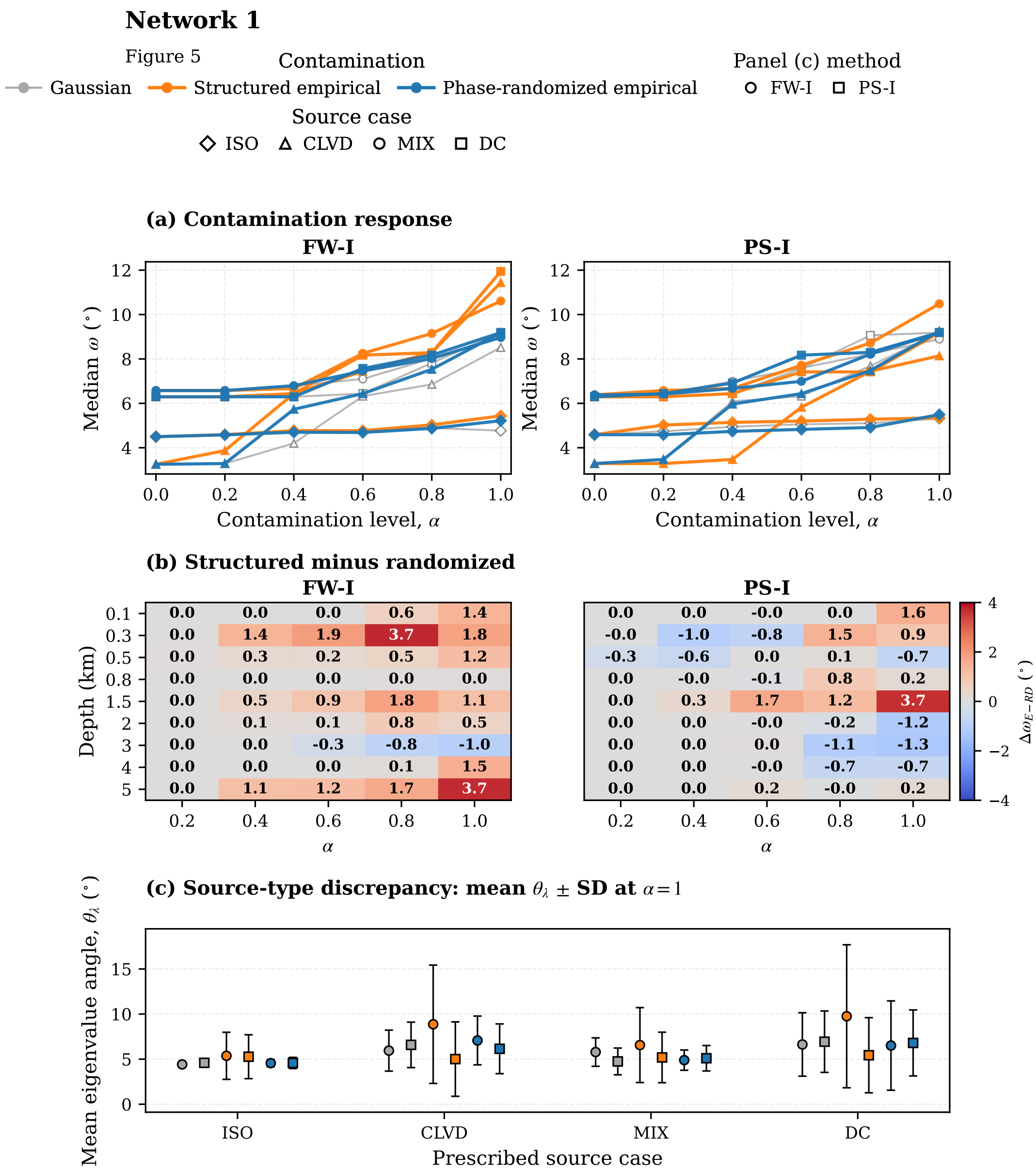

Figure 7. Role of temporal phase structure for Network 1. (a) Median ω as a function of contamination level for Gaussian, structured empirical, and phase-randomised empirical contamination under FW-I and PS-I. Gaussian contamination is shown as a stochastic reference. (b) Median paired structured-minus-randomised difference, $\Delta\omega_{E-RD} = \omega_{\text{structured}} - \omega_{\text{randomised}}$, for matched configurations. (c) Mean eigenvalue angle θ_λ at $\alpha = 1$ for the three contamination regimes; error bars denote ± 1 standard deviation across source-depth-orientation configurations after stochastic realisations are collapsed by their configuration-wise median.

Alt text: Multi-panel comparison of Gaussian, structured empirical, and phase-randomised empirical contamination for Network 1. Gaussian and phase-randomised results generally follow similar rotation-angle trends, whereas structured empirical contamination produces larger errors for selected source configurations under full-waveform inversion. Paired structured-minus-randomised depth differences vary in sign and magnitude, showing that the coherent effect is configuration dependent rather than uniform. P–S segmentation reduces most of these differences. The eigenvalue-angle response is weaker and more heterogeneous than the full-tensor rotation response.

changes. The detailed response is therefore a contaminant–source-depth–geometry interaction.

The 12-station configuration provides the clearest evidence for the stabilising role of observational redundancy. It substantially reduces structured-minus-Gaussian and structured-minus-randomised differences over most depths and also reduces the positive high-error tail documented in Section 3.1.4. Residual FW-I sensitivity remains at selected depths, so increased station coverage mitigates rather than eliminates structured mismatch.

3.1.6 *Sensitivity to Moment Tensor Constraint Strategy*

We performed a limited sensitivity analysis to examine how full moment tensor (FMT), deviatoric (DVT), and double-couple (DC) constraints redistribute inversion error under structured empirical

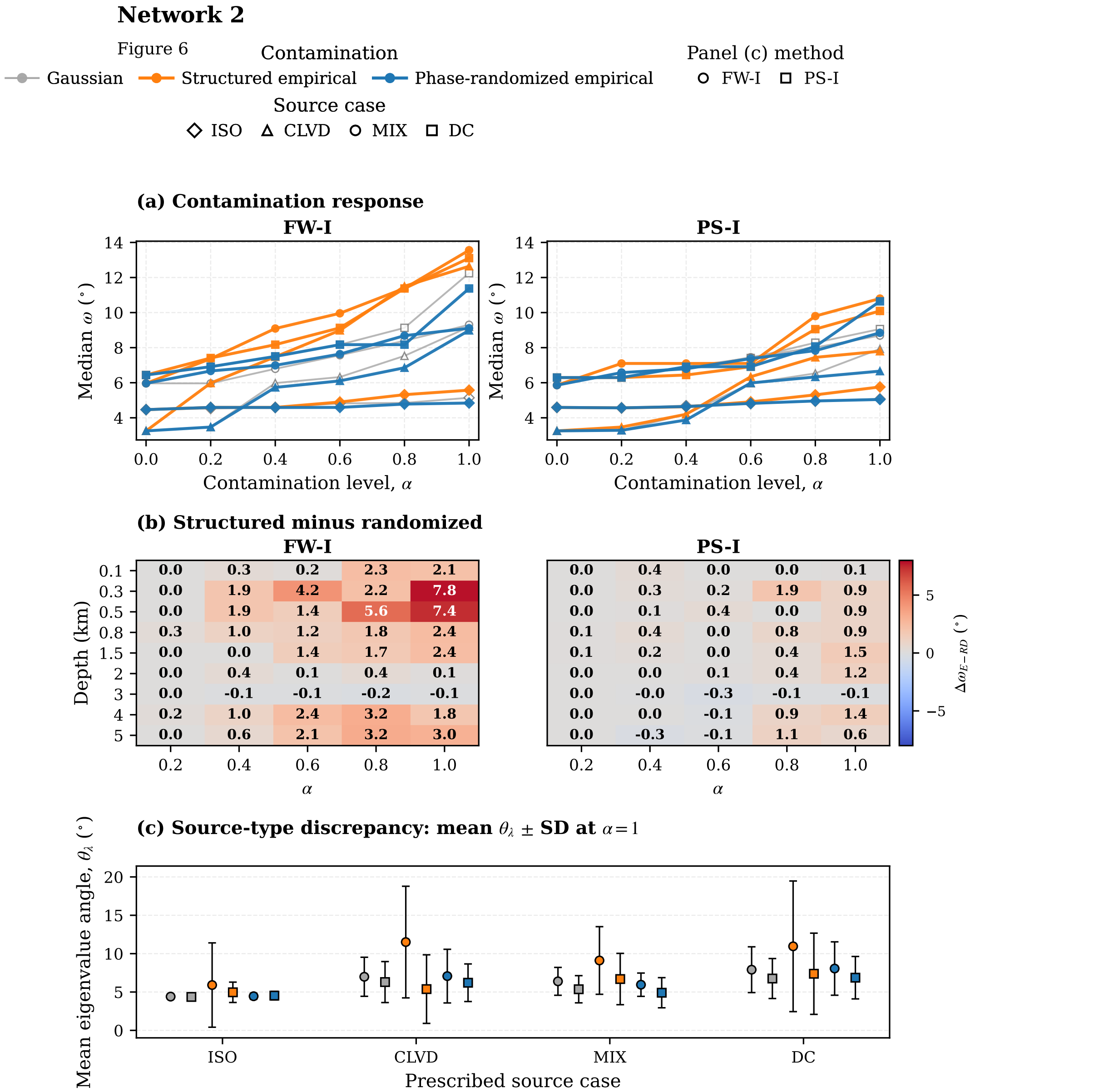

Figure 8. Role of temporal phase structure for Network 2. Panel definitions and statistical summaries are the same as in Fig. 7.

Alt text: Multi-panel comparison of Gaussian, structured empirical, and phase-randomised empirical contamination for Network 2. Gaussian and phase-randomised contamination produce similar ensemble-level behaviour, whereas structured empirical contamination generates larger full-waveform rotation errors for several non-ISO source cases. The paired structured-minus-randomised depth map shows the strongest positive excess in selected shallow configurations. P–S segmentation markedly reduces this response. Eigenvalue-angle differences indicate more selective source-type changes than the stronger full-tensor rotation changes.

contamination. Because the structured contaminant is deterministic for a given target configuration, variability in this experiment reflects differences among source configurations rather than stochastic repeatability.

Two complementary quantities are considered. Persistent mechanism bias is represented by the mean across contamination levels of the median rotation angle across matched configurations,

$$\overline{\omega} = \frac{1}{N_\alpha} \sum_\alpha \mathrm{median}_i[\omega_i(\alpha)], \tag{9}$$

whereas contamination sensitivity is represented by the paired increase

$$\Delta\omega_{0\to1} = \mathrm{median}_i[\omega_i(1) - \omega_i(0)]. \tag{10}$$

The resulting bias–sensitivity diagrams (Fig. 9) show that restrictive parametrisations can reduce the response to increasing contamination while simultaneously increasing absolute mechanism bias when the imposed constraint is incompatible with the prescribed source case. Compatible constraints generally occupy the low-bias part of the diagram, whereas incompatible DVT or DC parametrisations can produce relatively small $\Delta\omega_{0\to1}$ at large $\overline{\omega}$. The PS-I reduces the overall contamination sensitivity. Low sensitivity to increasing contamination is therefore not, by itself, evidence of reliable mechanism recovery.

3.2 Real-Data Illustration of Method-Dependent Depth Trade-off

To assess whether the synthetic diagnostics are relevant to observed mining-induced seismicity, we analysed one representative event recorded by the six-station Network 2 using the procedure described in Section 2.3.4. The example is diagnostic rather than descriptive and is used only to illustrate method-dependent depth non-uniqueness under realistic sparse-network conditions.

Fig. 10 shows the depth-dependent misfit and corresponding preferred full moment tensor solutions for the $M_L = 1.2$ event obtained with FW-I and PS-I. Both formulations favour a shallow minimum at approximately 0.5–0.8 km. The methods therefore do not select fundamentally different depth regimes, but they differ in the shape of the misfit surface and in the evolution of the preferred mechanism away from the minimum. FW-I shows larger changes in source character with tested depth, whereas PS-I preserves a more coherent mechanism family over a broader interval.

The selected moment magnitude also varies with tested depth, but the principal diagnostic information is the coupled dependence of misfit and recovered mechanism on source depth. The example is not used to infer a preferred physical mechanism or structural interpretation for this event.

4 DISCUSSION

The three-regime experiment separates stochastic degradation from structured waveform-induced bias and from the specific contribution of preserved temporal waveform organisation. Gaussian contamination defines the stochastic reference, while phase-randomised empirical contamination retains the empirical spectral amplitude but removes the original phase relationships. Their close ensemble-level correspondence contrasts with the more heterogeneous structured empirical response and shows that spectral amplitude alone does not reproduce the largest errors.

4.1 Structured Empirical Contamination and Waveform-Induced Bias

Structured empirical contamination produces larger full-tensor rotation errors than the stochastic controls for many susceptible configurations, particularly under FW-I. This behaviour is consistent with the distinction between observational variance and theory error in waveform inversion (Duputel et al., 2012; Phạm et al., 2024): temporally organised mismatch can be accommodated by changing source parameters rather than simply increasing residual variance.

The empirical perturbation should not be interpreted as a direct model of pure propagation error. Because it is itself a recorded seismic event, it contains source radiation together with propagation, scattering, attenuation, and site contributions. The additive experiment therefore represents a structured source–path–site wavefield superimposed on the target signal. It does not modify the Earth's transfer function; instead, it competes with the target waveform in a way that the inversion can partly absorb into the recovered source tensor.

Phase randomisation provides the key diagnostic. Preserving the empirical amplitude spectrum while destroying the original temporal organisation returns the ensemble-level response towards the Gaussian regime. The additional-contaminant tests further show that the coherence-related FW-I excess is reproducible across independent empirical waveforms, while its magnitude and depth localisation change with the contaminant. Preserved temporal organisation is therefore an important contributor to the largest structured-contamination errors, but the specific susceptible configurations are waveform-dependent.

4.2 Distributional Nature of Structured-Contamination Error

A central result of the distributional analysis is that structured contamination does not act primarily as a uniform increase in error. Many source–depth–orientation configurations remain weakly affected, producing modest configuration-level medians, while a smaller but substantial subset develops much larger rotation errors. Central statistics alone can therefore understate the practical susceptibility of an inversion configuration to structured waveform mismatch.

This behaviour persists when all 15 stochastic realisations are retained. Under FW-I, large positive structured-minus-Gaussian and structured-minus-randomised differences occur substantially more frequently than corresponding negative differences, particularly for Network 2. The asymmetry is therefore not created by reducing each stochastic population to its median. The within-configuration dominance analysis reaches the same conclusion: for many configurations the deterministic structured result exceeds most of the corresponding stochastic-control realisations.

The distributional perspective changes the interpretation of robustness. A network or inversion formulation with a small median paired difference can still contain a non-negligible population of high-error configurations. Robustness assessment should therefore consider both the typical response and the frequency of large errors. The 5° and 10° thresholds used here are diagnostic reference levels rather than universal quality criteria; the transferable principle is the explicit comparison of symmetric positive and negative tails.

4.3 Orientation and Source-Type Contributions to Moment-Tensor Error

The contrasting behaviour of ω and θ_λ helps identify how structured waveform mismatch is mapped into the recovered moment tensor. The rotation angle ω compares the complete tensors and is sensitive to changes in both eigenvector orientation and eigenvalue structure. By contrast, θ_λ compares only the normalised ordered eigenvalues and therefore isolates source-type discrepancy.

Structured empirical contamination produces a substantially stronger positive-tail enhancement in ω than in θ_λ, particularly under FW-I. This indicates that the largest coherence-related errors cannot generally be interpreted as source-type changes alone. A substantial component is associated with rotation of the recovered tensor orientation. Large changes in eigenvalue structure do occur, especially for selected CLVD-like, mixed, and DC configurations, but they are less systematic and are strongly reduced under PS-I.

This distinction is relevant when interpreting complex moment-tensor solutions in shallow environments. Structured waveform mismatch may substantially alter inferred fault orientation without producing an equally large displacement in source-type space. Conversely, a large θ_λ identifies the subset of cases in which the mismatch changes not only orientation but also the relative eigenvalue character of the recovered tensor.

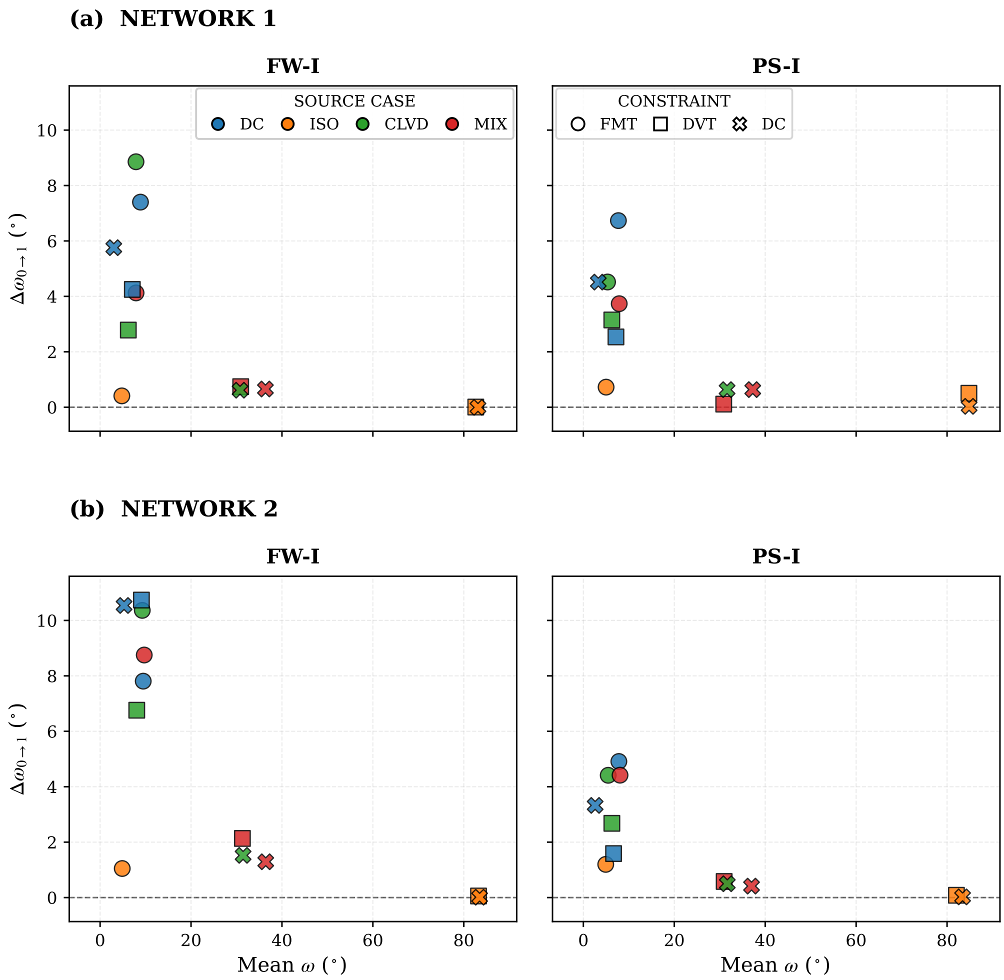

Figure 9. Bias–sensitivity trade-off for moment tensor constraint strategies under structured empirical contamination for Networks 1 and 2. The horizontal coordinate is the mean across contamination levels of the median rotation angle ω across matched source configurations and therefore represents persistent mechanism bias. The vertical coordinate is the median paired change $\Delta\omega_{0\to1} = \mathrm{median}_i[\omega_i(1) - \omega_i(0)]$. Colours identify the prescribed source case and symbols identify the inversion constraint (FMT, DVT, or DC). Large mean ω combined with small $\Delta\omega_{0\to1}$ denotes a solution that is relatively insensitive to increasing contamination but persistently biased.

Alt text: Bias–sensitivity diagrams comparing full moment tensor, deviatoric, and double-couple inversion constraints under structured empirical contamination. Each point represents a prescribed source case and inversion constraint. The horizontal axis measures persistent moment-tensor rotation bias across contamination levels, and the vertical axis measures the paired increase in rotation from the uncontaminated to the most contaminated case. Compatible constraints generally occupy the low-bias region, whereas some incompatible restrictive constraints show low contamination sensitivity but large persistent bias, demonstrating that apparent stability does not necessarily imply accurate source recovery.

4.4 Effect of Station Coverage Under Structured Contamination

The 12-station experiment demonstrates that increased observational redundancy reduces both central error and high-error susceptibility. Relative to the six-station networks, the combined configuration suppresses much of the structured-minus-Gaussian and structured-minus-randomised excess over the tested depth range. Under FW-I, the probability of a structured-minus-randomised rotation difference greater than 5° decreases to 15.9 per cent, compared with 23.4 per cent for Network 1 and 32.1 per cent for Network 2; the corresponding $> 10°$ probability falls to 4.3 per cent.

The stabilising effect should not be interpreted simply as averaging random noise. A denser network changes azimuthal sampling, take-off-angle coverage, station weighting, and the degree to which a particular coherent waveform pattern can be fit consistently across the observations. A contaminant that favours an incorrect source tensor for a sparse geometry may become internally inconsistent when additional stations are included. Residual FW-I sensitivity nevertheless remains, so station count alone does not guarantee immunity to structured waveform mismatch.

4.5 Method Dependence and the Role of P–S Segmentation

Waveform-segmentation strategies derived from the Cut-and-Paste framework improve tolerance to timing mismatch by allowing distinct waveform groups to be aligned independently (Zhao & Helmberger, 1994; Zhu & Helmberger, 1996). The PS-I formulation used here follows this principle within a full moment tensor search by treating the P- and S-wave windows as independent contributions with separate timing adjustments.

The distributional analysis clarifies the main benefit of PS-I.

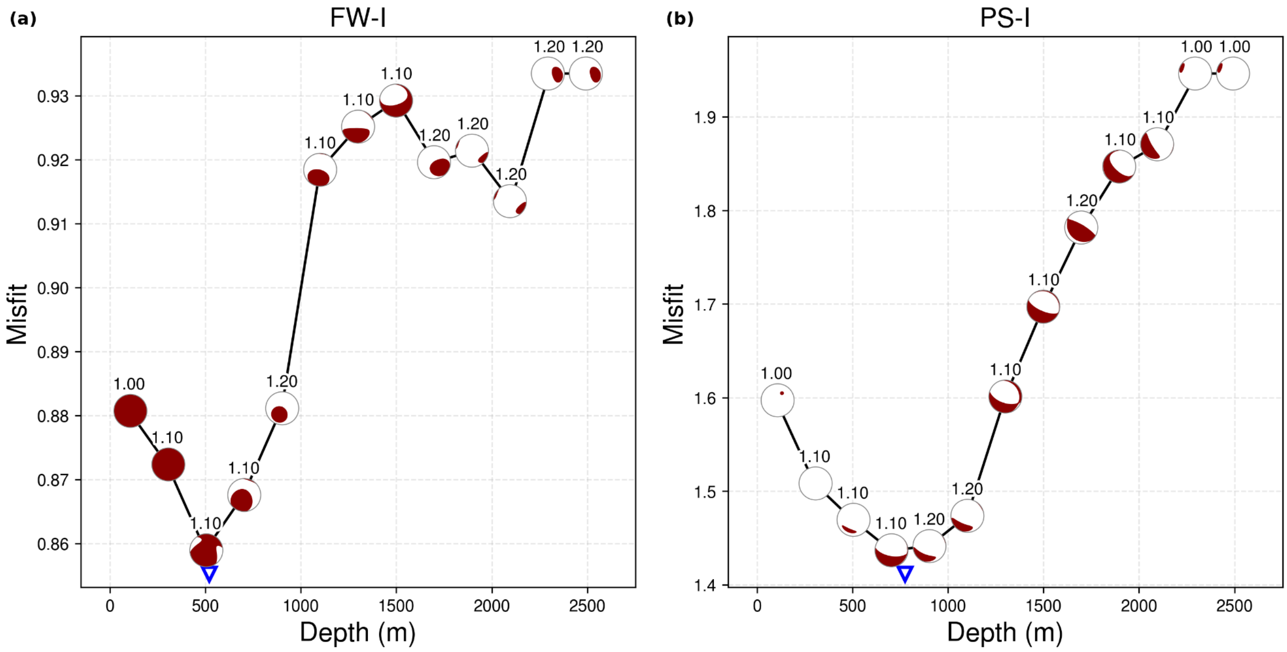

Figure 10. Real-data depth-trade-off illustration for a representative $M_L = 1.2$ event recorded by Network 2 using (a) full-waveform inversion (FW-I) and (b) P–S segmented inversion (PS-I). The black curve shows waveform misfit as a function of tested source depth, and the inverted triangle marks the minimum-misfit depth. Beachballs show the preferred full moment tensor at each tested depth, with the corresponding moment magnitude indicated above each solution. The example is presented only as a diagnostic illustration of method- and depth-dependent non-uniqueness and is not used to infer a preferred physical source mechanism.

Under FW-I, structured empirical contamination produces a pronounced positive high-error tail relative to the stochastic controls. Under PS-I, the positive and negative tails become much more balanced and the frequency of large positive differences falls markedly. For Network 2, for example, the structured-minus-randomised probability above $+5^\circ$ decreases from 32.1 per cent under FW-I to 14.3 per cent under PS-I. In the 12-station case it decreases further to 3.1 per cent, with no differences above $+10^\circ$.

PS-I therefore does more than reduce a median error: it decreases the likelihood that differential mismatch between P- and S-wave packets is mapped into a large full-tensor rotation. The improvement is not universal, and phase randomisation can redistribute contaminant energy between the subsequently extracted P and S windows. For this reason the FW-I structured-versus-randomised comparison remains the cleanest direct diagnostic of temporal phase organisation, whereas PS-I shows how segmentation modifies its expression.

4.6 Depth Dependence as a Contaminant–Geometry Interaction

The experiments do not support a universal depth at which structured empirical contamination becomes most damaging. For the main contaminant, both six-station networks show pronounced shallow FW-I sensitivity, whereas the additional-contaminant tests demonstrate that the depth of maximum coherent-minus-randomised excess can migrate among 0.5, 2, and 4 km.

This behaviour follows naturally from the experimental construction. The same contaminating waveform is superimposed on target synthetics generated at multiple source depths. Changing the target depth modifies travel times, waveform shape, take-off angles, relative phase timing, and the set of source tensors capable of fitting the resulting contaminated waveform. Depth is therefore one axis of a higher-dimensional interaction involving target mechanism, contaminant waveform, network geometry, and inversion formulation. A problem depth identified for one contaminant should not be transferred directly to another event or network.

4.7 Sensitivity to Moment Tensor Constraint Strategy

The constraint experiment separates persistent mechanism bias from sensitivity to increasing structured contamination. Restricting the admissible model space can reduce $\Delta\omega_{0\rightarrow 1}$, but this does not guarantee that the restricted solution is closer to the prescribed tensor. When the imposed constraint is incompatible with the source, the solution can remain comparatively insensitive to increasing contamination while being strongly biased at all contamination levels.

Stability under perturbation and accuracy with respect to the true source are therefore distinct properties. A tightly constrained inversion may appear robust because its model space does not permit substantial movement, even though the resulting mechanism is systematically incorrect. Constraint selection should be guided by physically defensible source assumptions and evaluated using both absolute bias and perturbation sensitivity.

4.8 Real-Data Illustration and Diagnostic Consistency

The real-data example provides a practical extension of the synthetic diagnostics. In the synthetic tests, depth is prescribed and contamination can be evaluated against a known tensor. In real data, source depth is itself uncertain; comparable sensitivity therefore appears as a depth trade-off in which several tested depths can provide acceptable waveform fits while producing different source tensors.

Both FW-I and PS-I favour a similar shallow depth interval for the representative event, but FW-I shows stronger mechanism variability as tested depth moves away from the minimum, whereas PS-I preserves a more coherent mechanism family over a broader interval. The example is deliberately not used to validate a particular synthetic error magnitude or to infer the physical mechanism of the event. It shows only that method- and depth-dependent non-uniqueness of the type diagnosed synthetically is present in the sparse local data.

4.9 A Transferable Stress-Testing Framework for Shallow MTI

The experiments define a practical stress-testing framework for MTI in shallow and structurally complex seismic environments. Although the numerical error levels obtained for Jacobina are site-specific, the diagnostic sequence is transferable. Its required inputs are an operational station configuration, a plausible source-depth range, representative source types, and locally recorded events suitable for constructing structured empirical perturbations. A stochastic reference is first established using band-limited Gaussian contamination. Structured empirical contamination is then introduced to test whether solutions that appear stable under random perturbations remain robust to temporally organised source–path–site waveform mismatch. Finally, phase randomisation of the same empirical records, while preserving their Fourier-amplitude spectra, provides a control for the contribution of temporal waveform organisation.

Robustness is evaluated using both central and distributional measures. Configuration-level statistics characterise the typical response, whereas quantiles and two-sided exceedance probabilities identify susceptibility to large-error outcomes that may be obscured by small median differences. Repeating the structured-versus-randomised comparison with independent empirical contaminants further tests whether the observed response is tied to a particular waveform. The same framework can be used to evaluate mitigation strategies: additional stations test the benefit of spatial redundancy, phase-segmented formulations test sensitivity to differential timing mismatch, and source constraints expose the trade-off between reduced perturbation sensitivity and persistent model bias. Station- or phase-specific corrections and empirical Green's functions (Hartzell, 1978; Mueller, 1985) could be assessed within the same diagnostic sequence.

The workflow is intended as a diagnostic stress test rather than a complete probabilistic uncertainty model. Its practical purpose is to determine whether an MTI configuration is robust only to unstructured waveform variance or also to the structured mismatch expected in shallow complex environments, and whether modifications to network design, waveform treatment, or source parameterisation reduce that susceptibility.

5 CONCLUSIONS

This study presents a controlled diagnostic assessment of moment tensor inversion under Gaussian, structured empirical, and phase-randomised empirical waveform contamination for shallow mining-induced seismicity. Gaussian and phase-randomised contamination produce similar ensemble-level behaviour, whereas structured empirical contamination produces a more heterogeneous response that is not adequately described by central statistics alone.

Under FW-I, the principal structured-contamination effect is a positive high-error asymmetry in the paired rotation distribution: many configurations remain weakly affected, but a susceptible subset develops substantially larger full-tensor errors than under Gaussian or phase-randomised controls. The persistence of this behaviour when all 15 stochastic realisations are retained shows that it is not an artefact of configuration-wise median aggregation. Phase randomisation substantially reduces the high-error excess, demonstrating that preserved temporal waveform organisation is important to its development.

The contrast between the full-tensor rotation ω and the eigenvalue angle θ_λ further shows that the effect is not purely a source-type change. Source-type discrepancies also develop an enhanced positive tail under FW-I, particularly for some non-ISO configurations, but the response is weaker and less systematic than for ω. A substantial component of the structured-contamination error is therefore associated with changes in recovered tensor orientation.

P–S segmentation and increased station coverage both reduce high-error susceptibility. PS-I markedly suppresses the positive ω tail, while the 12-station configuration reduces both the median structured-contamination excess and the frequency of large positive differences. Neither strategy guarantees complete immunity to structured mismatch, and their effectiveness remains configuration-dependent. Constraint tests additionally demonstrate that low sensitivity to contamination can coexist with large persistent source bias when an inappropriate source model is imposed.

The additional-contaminant tests show that the coherence-related FW-I excess is reproducible across independent empirical waveforms, while the depth and configuration of maximum susceptibility vary. Detailed depth patterns should therefore be interpreted as contaminant–source–geometry interactions rather than universal depth effects.

More generally, the experiments define a transferable diagnostic framework for stress-testing shallow MTI before interpreting field solutions. The framework combines a stochastic reference, representative structured empirical contamination, phase-randomised controls, paired configuration analysis, explicit evaluation of large-error tails, and tests of acquisition or inversion mitigation. The numerical thresholds are site-specific, but the diagnostic sequence can be adapted to other shallow and structurally complex seismic environments.

ACKNOWLEDGEMENTS

The authors thank the staff of the Seismological Laboratory of the Federal University of Rio Grande do Norte (LabSis/UFRN) for assistance with the deployment, maintenance, and operation of the temporary seismic networks and with waveform-data management. This study was supported by the National Institute of Science and Technology for Tectonic Studies (INCT-Tectônicos) under CNPq grant number 465613/2014-4. S. G. Gomes acknowledges support from Fundação de Apoio ao Desenvolvimento da Computação Científica (FACC), through a research fellowship granted under the project Brazilian Seismographic Network (RSBR) / CPRM-ON-UFRN. A. F. do Nascimento thanks CNPq for his PQ grant 312884/2021-4.

During preparation of this manuscript, the authors used OpenAI ChatGPT and SciSpace AI to assist with language editing, manuscript organisation and document formatting. These tools

were not used to generate the underlying seismic data, inversion results or figures. All AI-assisted text was reviewed and edited by the authors, who take full responsibility for the manuscript.

Conflicts of interest: The authors declare no conflicts of interest.

DATA AVAILABILITY

The numerical results underlying the main and supplementary figures, the machine-readable parameter tables, the synthetic-test configuration files, and the scripts used for waveform contamination, phase randomisation, inversion processing, data summarization, and figure generation are archived in Zenodo at https://doi.org/10.5281/zenodo.22239316 ([dataset] Gomes et al., 2026).

The raw continuous waveform data and detailed station and mining-site metadata are not publicly available because they are subject to ongoing-study and data-use restrictions. Access is administered by LabSis/UFRN and requires prior written authorisation from the relevant data owner. These restrictions do not apply to the synthetic results, scripts, and derived numerical products deposited in Zenodo.

REFERENCES

Barbosa, J. S. F. & Sabaté, P., 2004. Archean and Paleoproterozoic crust of the São Francisco Craton, Bahia, Brazil: geodynamic features, *Precambrian Research*, **133**, 1–27.

Barthwal, H. & van der Baan, M., 2020. Microseismicity observed in an underground mine: Source mechanisms and possible causes, *Geomechanics for Energy and the Environment*, **22**, 100167. doi: 10.1016/j.gete.2019.100167.

Birnie, C., Chambers, K., Angus, D., & Stork, A. L., 2020. On the importance of benchmarking algorithms under realistic noise conditions, *Geophysical Journal International*, **221**, 504–520. doi: 10.1093/gji/ggaa025.

Caputa, A., Rudziński, L., & Cesca, S., 2021. How to assess the moment tensor inversion resolution for mining-induced seismicity: a case study for the Rudna mine, Poland, *Frontiers in Earth Science*, **9**, 671207. doi: 10.3389/feart.2021.671207.

Chang, Y., Warren, L. M., Zhu, L., & Prieto, G. A., 2019. Earthquake focal mechanisms and stress field for the intermediate-depth Cauca cluster, Colombia, *Journal of Geophysical Research: Solid Earth*, **124**, 822–836. doi: 10.1029/2018JB016804.

[dataset] Gomes, S. G., do Nascimento, A. F., Leite Neto, G. S., Fonsêca, J. A. S., Menezes, E. A. S., & Fuck, R. A., 2026. Numerical results, scripts and reproducibility material for "Structured empirical waveform contamination in moment tensor inversion of shallow mining seismicity: A synthetic diagnostic framework". Zenodo. doi: 10.5281/zenodo.22239316, Version 2.0.0.

Duputel, Z., Rivera, L., Fukahata, Y., & Kanamori, H., 2012. Uncertainty estimations for seismic source inversions, *Geophysical Journal International*, **190**, 1243–1256. doi: 10.1111/j.1365-246X.2012.05554.x.

Gibowicz, S. J. & Kijko, A., 1994. *An Introduction to Mining Seismology*, Academic Press, San Diego.

Gibowicz, S. J. & Lasocki, S., 2001. Seismicity induced by mining: ten years later, *Advances in Geophysics*. doi: 10.1016/S0065-2687(00)80007-2.

Hartzell, S. H., 1978. Earthquake aftershocks as Green's functions, *Geophysical Research Letters*, **5**, 1–4. doi: 10.1029/GL005i001p00001.

Havskov, J. & Ottemöller, L., 1999. SEISAN earthquake analysis software, *Seismological Research Letters*, **70**, 532–534. doi: 10.1785/gssrl.70.5.532.

Herrmann, R. B., 2013. Computer Programs in Seismology: an evolving tool for instruction and research, *Seismological Research Letters*, **84**, 1081–1088. doi: 10.1785/0220110096.

Lienert, B. R. & Havskov, J., 1995. A computer program for locating earthquakes both locally and globally, *Seismological Research Letters*, **66**, 26–36. doi: 10.1785/gssrl.66.5.26.

Lizurek, G., 2017. Full moment tensor inversion as a practical tool in case of discrimination of tectonic and anthropogenic seismicity in Poland, *Pure and Applied Geophysics*, **44**, 39–81. doi: 10.1007/s00024-016-1378-9.

Ma, J., Dong, L., Zhao, G., & Li, X., 2019. Focal mechanism of mining-induced seismicity in fault zones: a case study of Yongshaba mine in China, *Rock Mechanics and Rock Engineering*, **52**, 3341–3352. doi: 10.1007/s00603-019-01761-4.

Mueller, C. S., 1985. Source pulse enhancement by deconvolution of empirical Green's functions, *Geophysical Research Letters*, **12**, 33–36. doi: 10.1029/GL012i001p00033.

Phạm, T.-S., Tkalčić, H., Hu, J., & Kim, S., 2024. Towards a new standard for seismic moment tensor inversion containing 3-D earth structure uncertainty, *Geophysical Journal International*, **238**, 1840–1853. doi: 10.1093/gji/ggae256.

Santos, F. P., Chemale Junior, F., & Meneses, A. R., 2019. The nature of the Paleoproterozoic orogen in the Jacobina Range and adjacent areas, northern São Francisco Craton, Brazil, based on structural geology and gravimetric modelling, *Precambrian Research*, **332**, 105391. doi: 10.1016/j.precamres.2019.105391.

Tape, W. & Tape, C., 2012. Angle between principal axis triples, *Geophysical Journal International*, **191**, 813–831. doi: 10.1111/j.1365-246X.2012.05658.x.

Tape, W. & Tape, C., 2019. The eigenvalue lune as a window on moment tensors, *Geophysical Journal International*, **216**, 19–33. doi: 10.1093/gji/ggy373.

Thurin, J., Modrak, R., Tape, C., McPherson, A. M., Rodríguez-Cardozo, F. R., Kintner, J., Ding, L., Liu, Q., & Braunmiller, J., 2025. MTUQ: a framework for estimating moment tensors, point forces, and their uncertainties, *Geophysical Journal International*, **241**, 1373–1390. doi: 10.1093/gji/ggaf080.

Vavryčuk, V. & Kühn, D., 2012. Moment tensor inversion of waveforms: a two-step time-frequency approach, *Geophysical Journal International*, **190**, 1761–1776. doi: 10.1111/j.1365-246X.2012.05592.x.

Vuan, A., Sugan, M., Amat, G., & Kato, A., 2018. Improving the detection of low-magnitude seismicity preceding the M_W 6.3 L'Aquila earthquake: development of a scalable code based on the cross-correlation of template earthquakes, *Bulletin of the Seismological Society of America*, **108**, 471–480. doi: 10.1785/0120170106.

Waldhauser, F. & Ellsworth, W. L., 2000. A double-difference earthquake location algorithm: method and application to the northern Hayward fault, California, *Bulletin of the Seismological Society of America*, **90**, 1353–1368. doi: 10.1785/0120000006.

Zhao, L.-S. & Helmberger, D. V., 1994. Source estimation from broadband regional seismograms, *Bulletin of the Seismological Society of America*, **84**, 91–104.

Zhu, L. & Helmberger, D. V., 1996. Advancement in source estimation techniques using broadband regional seismograms, *Bulletin of the Seismological Society of America*, **86**, 1634–1641.